HIGH-RESOLUTION TIME-RESOLVED IMAGING SYSTEM IN THE VACUUM ULTRAVIOLET REGION

by

YUSEONG JANG
B.S. Hanyang University, 2009
M.S. Hanyang University, 2012

A thesis submitted in partial fulfillment of the requirements
for the degree of Master of Science
in the College of Optics and Photonics
at the University of Central Florida
Orlando, Florida

Summer Term
2014

© 2014 Yuseong Jang

ABSTRACT

High-power debris-free vacuum ultraviolet (VUV) light sources have applications in several scientific and engineering areas, such as high volume manufacturing lithography and inspection tools in the semiconductor industry, as well as other applications in material processing and photochemistry.

For the past decades, the semiconductor industry has been driven by what is called "Moore's Law". The entire semiconductor industry relies on this rule, which requires chip makers to pack transistors more tightly with every new generation of chips, shrinking the size of transistors. The ability to solve roadmap challenges is, at least partly, proportional to our ability to measure them. The focus of this thesis is on imaging transient VUV laser plasma sources with specialized reflective imaging optics for metrology applications. The plasma dynamics in novel laser-based Zinc and Tin plasma sources will be discussed. The Schwarzschild optical system was installed to investigate the time evolution of the plasma size in the VUV region at wavelengths of 172 nm and 194 nm. The outcomes are valuable for interpreting the dynamics of low-temperature plasma and to optimize laser-based VUV light sources.

ACKNOWLEDGMENTS

I would wish to gratefully thank Dr. Martin Richardson for giving me the opportunity and support, and encouragement to perform this project. Likewise, I thank the committee members, Dr. Patrick Likamwa and Dr. Jim Moharam for being my committee members and spending time on my thesis.

I desire to thank EUV team, Dr. Majid Masnavi, Dr. Homaira Parchamy, John Szilagyi for discussions and support, and all LPL members, especially, Nathan Bodnar, Joshua Bradford, Cheonha Jeon for help. Also, thank Richard Zotti for teaching and helping me how to construct my system in a machine shop.

At last, not least, I like to acknowledge my parents and kin.

TABLE OF CONTENTS

LIST OF FIGURES vii

LIST OF TABLES x

LIST OF ABBREVIATIONS xi

INTRODUCTION 1

CHAPTER 1: IMAGING SYSTEMS FOR SHORT WAVELENGTHS 3

1.1 Grazing Incidence Reflective Optics 3

1.2 Normal Incidence Reflective Optics 7

1.3 Refractive Optics 10

1.4 Diffractive Optics 11

CHAPTER 2: OPTICAL SYSTEM 16

2.1 Schwarzschild Objective Ray Tracing 16

2.2 Spider Diffractions in Schwarzschild 21

2.3 Mirror Coatings 23

2.4 Optical Bandpass Filter 25

CHAPTER 3: EXPERIMENTAL APPARATUS 26

3.1 Intensified charge-coupled devices 26

3.2 Photon budgets 28

3.3 Timing 29

3.4 Degrees of Freedom 31

3.5 Sensitivity of Adjustments 33

CHAPTER 4: RESULTS 35

4.1 Imaging System Analysis 35

4.2 Plasma Images 36

4.3 Plasma Dynamics and Input intensity Dependencies 38

CHAPTER 5: CONCLUSIONS 43

LIST OF REFERENCES 44

LIST OF FIGURES

Figure 1 X-ray image by Wilhelm Conard Röntgen 1

Figure 2 Kirkpatrick-Baez mirrors congifuation 4

Figure 3 Wolter optics: type I (a) telescope (b) microscope; type II (c) telescope (d) microscope; type III (e) telescope 6

Figure 4 Montel optics 7

Figure 5 Schwarzschild objective 8

Figure 6 Diagram of Multi-layers for high reflection 9

Figure 7 Reflectivity of Si/Mo multilayer with stack numbers at normal incidence [25] 10

Figure 8 Single CRL 11

Figure 9 Planar diffraction grating 12

Figure 10 Concave diffraction grating 13

Figure 11 Aberration-corrected concave grating 13

Figure 12 Diffracting Fresnel Zone plate 14

Figure 13 Spot diagrams with Airy disks in the image plane with different object height, on-axis (left) and 100 µm from the axis (right) 19

Figure 14 Modulation transfer function (MTF) 21

Figure 15 Diffraction effects of secondary mirror spiders on image quality [38] 22

Figure 16 Images of different pinhole sizes *D* = (a) 10 µm, (b) 50 µm, and (c) 100 µm 22

Figure 17 Transmission of MgF_2 window 24

Figure 18 Reflectivity of Al/MgF_2 coating 24

Figure 19 Transmissions of bandpass filters 25

Figure 20 Schematic diagram of ICCD 27

Figure 21 Quantum efficiency of the ICCD 27

Figure 22 Sn and Zn spectral irradiance with different input laser powers at 0.8 m 28

Figure 23 Total calculated efficiency of the whole system 29

Figure 24 Schematic of experimental setup 30

Figure 25 Measured timing diagram 31

Figure 26 (a) Diagram of MgF_2 dimension, (b) procedure of how to glue the secondary mirror on MgF_2 window, (c) picture of mold, and (d) convex mirror glued to the MgF_2 window 32

Figure 27 Experimental setup 33

Figure 28 Spot diagrams with 10° rotations of knobs of (a) secondary, (b) primary tip/tilt, and (c) a 0.1 mm distance variation of the primary mirror in Z-direction 34

Figure 29 Resolution chart image and Deuterium lamp spectrum [42] 35

Figure 30 Zn target plasma images with 172 nm filter 36

Figure 31 Zn target plasma with 194 nm filter 37

Figure 32 Sn target plasma images with 172 nm filter 37

Figure 33 Sn target plasma images with 194 nm filter 38

Figure 34 Lowest intensity Zn plasma images in a same scale and transient plasma maximum intensities with different input laser intensities 39

Figure 35 Horizontal and vertical Zn plasma diameters in a time domain 39

Figure 36 Ouput/input ratio and maximum diameters of Zn plasmas in terms of input laser intensities 40

Figure 37 Lowest intensity Sn plasma images in a same scale and transient plasma maximum intensities with different input laser intensities 41

Figure 38 Horizontal and vertical Sn plasma diameters in a time domain 41

Figure 39 Ouput/input ratio and maximum diameters of Sn plasmas in terms of input laser intensities 42

LIST OF TABLES

Table 1 Specification of Schwarzschild objective 18

LIST OF ABBREVIATIONS

CCD	charge coupled device
CE	conversion efficiency
CO	central obstruction
CRLs	compound refractive lenses
DPP	discharge produced plasma
DUV	deep ultraviolet
EUV	extreme ultraviolet
FPS	frames per second
LPL	laser plasma laboratory
LPP	laser produced plasma
ICCD	intensified CCD
MCP	microchannel plate
MFT	modulation transfer function
ML	multi-layer
NA	numerical aperture
OPD	optical path difference
TPI	thread per inch

INTRODUCTION

The development of light sources has led to valuable applications in scientific discipline and engineering area. After an X-ray was discovered by Wilhelm Conard Röntgen in 1895 [1] with an image of his wife's ring-bearing hand shown in Figure 1, scientific advances had been achieved such as X-ray diffraction by crystal structure [2, 3]. Over time, X-ray optics have been improved. The development of these optics has led to the possibility of using short wavelength light to improve image resolutions.

Figure 1 X-ray image by Wilhelm Conard Röntgen

An Extreme ultraviolet (EUV) light source has been developed with the available mirror coatings at 13.5 nm wavelength [4, 5] following "Moore's law" in semiconductor industries. Many efforts for the realization of EUV lithography have been made [6, 7, 8, 9, 10, 11, 12] since it was anticipated that the current lithography at 193 nm wavelength meets the technical and cost saturation with an NA of 1.35 [13].

A Vacuum ultraviolet (VUV) refers to the wavelength ranges from 10 to 200 nm. The name originated from the fact that the spectral region is absorbed by air. The light in the VUV range should be used in a vacuum environment. The VUV radiations can be utilized for both bare and patterned wafer inspections by scattering. The intensity of scattered light is inversely proportional to its wavelength to the power of 4. Therefore, the shorter wavelength light source development is desirable. In that respect, there are several VUV light sources: arc lamps, excimer lasers (193 nm), and laser-induced plasma sources. However, they have disadvantages: arc lamps use electrodes that erode fast, current excimer lasers cannot provide high enough power, and laser-induced plasmas need to find the optimum conditions for enough power and sizes [14].

In this thesis, an imaging system is described and demonstrated to investigate the laser-induced plasma in the VUV region. Several types of X-ray imaging optics are reviewed in CHAPTER 1. In CHAPTER 2, the ray tracing of a Schwarzschild objective and mirror coatings are explained and CHAPTER 3 introduces the experimental setup, including the intensified charge-coupled detection device, the photon budget, and timing issues. The experimental results are explained in CHAPTER 4. In Chapter 5, improvements that can be made and applications that can ensue are speculated.

CHAPTER 1: IMAGING SYSTEMS FOR SHORT WAVELENGTHS

X-rays are the electromagnetic waves with photon energies between 100 eV (12.4 nm) and 100 keV (0.01 nm). The X-rays with photon energies below and higher than 10 keV (0.12 nm) are called soft and hard X-rays respectively [15]. Soft X-rays are highly absorbed in conventional visible optics while hard X-rays are penetrable in materials. The characteristics of X-rays having short wavelengths and high penetrations into materials, lead to many imaging applications in the field of medicine [16] and material characterizations [2, 3]. The optics used for the short wavelength, mostly soft X-rays, will be discussed in this chapter.

1.1 Grazing Incidence Reflective Optics

A reflectivity of s- and p-polarized electromagnetic waves at an interface between two different materials is expressed by Fresnel equation [17],

$$R_s = \left| \frac{n_1 cos\theta_i - n_2\sqrt{1-\left(\frac{n_1}{n_2} sin\theta_i\right)^2}}{n_1 cos\theta_i + n_2\sqrt{1-\left(\frac{n_1}{n_2} sin\theta_i\right)^2}} \right|^2, \quad (1)$$

$$R_p = \left| \frac{n_1\sqrt{1-\left(\frac{n_1}{n_2} sin\theta_i\right)^2} - n_2 cos\theta_i}{n_1\sqrt{1-\left(\frac{n_1}{n_2} sin\theta_i\right)^2} + n_2 cos\theta_i} \right|^2, \quad (2)$$

where $n_{1,2}$ are refractive indices of incident and transmitted regions, respectively, and θ_i is an incident angle. The reflectivity increases as an incident angle increases. Kirkpatrick-Baez optics [18], Wolter optics [19], and Montel optics [20] are examples of grazing incidence reflective optics.

The Kirkpatrick-Baez (KB) optics is comprised of two elliptic-cylindrical mirrors. The schematic diagram is shown in Figure 2. Each mirror focuses the beam in one direction: a first mirror (vertical) focuses a sagittal plane while a second mirror (horizontal) focuses a tangential plane. The elliptical surfaces focus one of two focal points onto the other focal point.

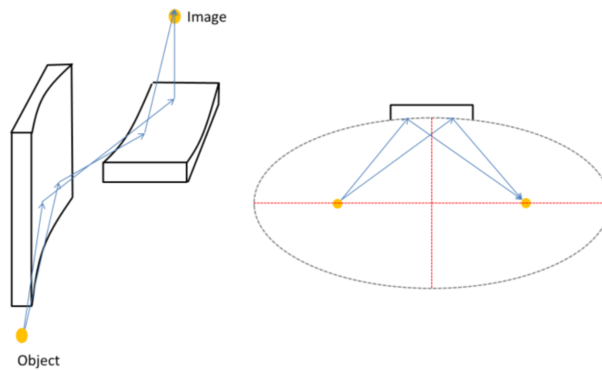

Figure 2 Kirkpatrick-Baez mirrors congifuation

Wolter optics are combinations of two mirrors from hyperbola, parabola, and elliptical mirrors. There are three types of Wolter optics and the cross sections of the optics are shown in Figure 3. Case I and II can focus far or near field depending on the choice of the first mirror: the far field is focused by a parabolic mirror (telescope) while the near field (microscope) is focused by an elliptical mirror. Type I consists of a parabolic or an elliptical mirror and a hyperbolic mirror. The first mirror reflects an incident ray to a focal point of the parabola (or ellipse) surface. The reflected beam then enters the second mirror and is focused to a focal point inside the hyperbola surface. In case II, the second mirror reflects the incoming ray to the focal point that is outside the

hyperbola surface. There is no microscopic function in Type III, which is the combination of a hyperbolic and an elliptical mirror.

Montel optics is also called "side-by-side" optics due to the fact that the edges of two mirrors meet in mutually perpendicular ways. Each surface of the mirrors has an elliptic cylinder shaped as it is shown in Figure 4. Incident rays are reflected on one of the mirrors and then reflected onto the other outer surface to be focused to a focal point. This type of optics needs an aperture to block rays not reflected by either of the two surfaces.

Type I

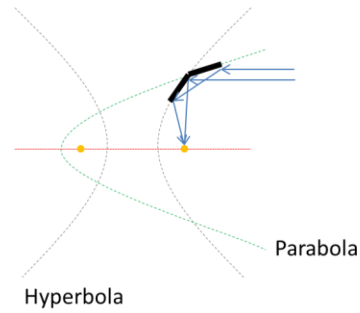

(a) telescope

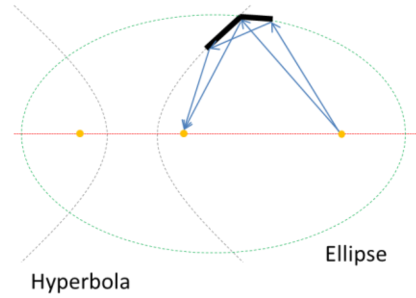

(b) microscope

Type II

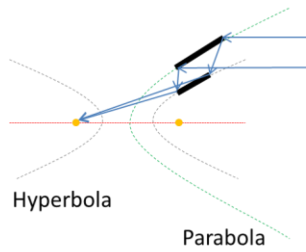

(c) telescope

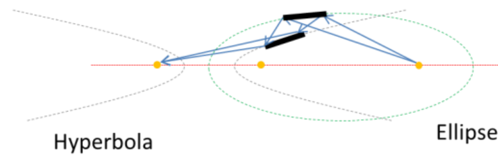

(d) microscope

Type III

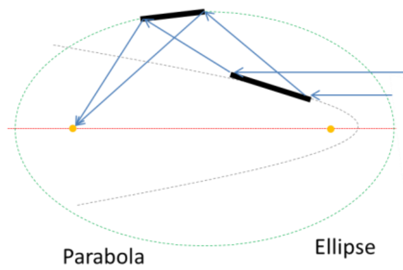

(e) telescope

Figure 3 Wolter optics: type I (a) telescope (b) microscope; type II (c) telescope (d) microscope; type III (e) telescope

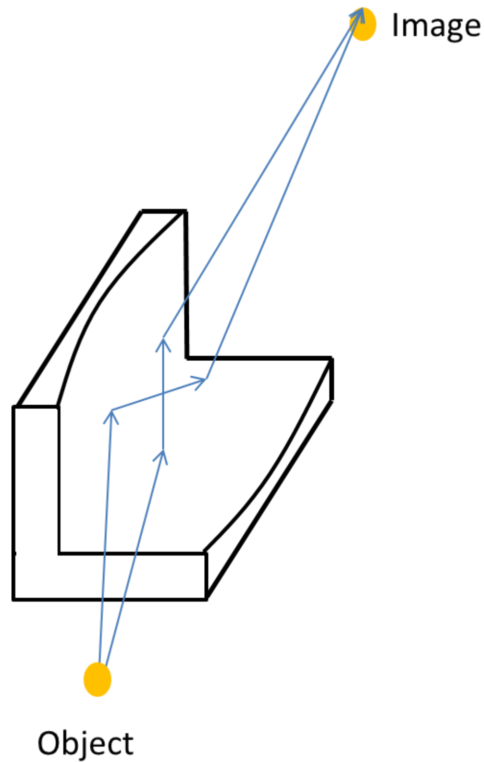

Figure 4 Montel optics

1.2 Normal Incidence Reflective Optics

Other than the grazing incidence optics, a normal incidence optics, Schwarzschild type [21] with multi-layer pair coating, is also used for soft X-ray or extreme ultraviolet (EUV) imaging. Schwarzschild optics employ two concentric spherical mirrors with a hole in the primary mirror. This case gives the simplest reflective optical system with low geometrical aberrations [22]. If two mirrors are not concentric with a hole in the primary mirror, the optical design is called Cassegrain [23]. The Schwarzschild is a special case of Cassegrain objective.

An object is magnified or minified depending on mirror positions. When an object is located prior to the primary mirror as shown in Figure 5, an image is magnified with a decrease in a numerical aperture (NA). If an object is located behind the primary mirror, an image is minified.

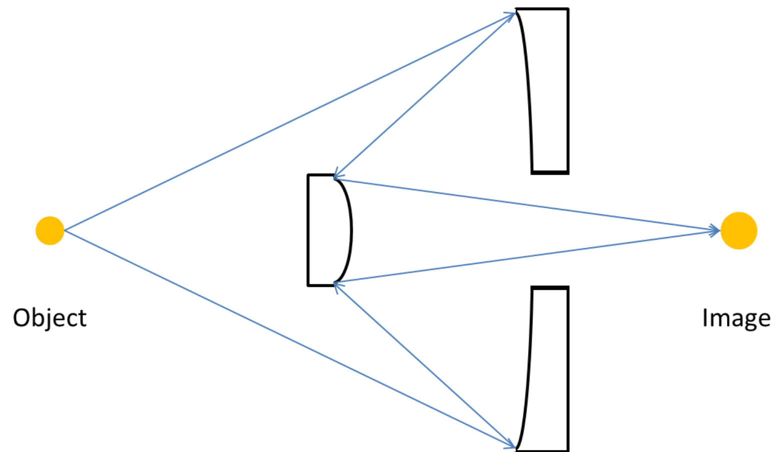

Figure 5 Schwarzschild objective

A multi-layer (ML) coating is based on a high-reflection coating [24]. Figure 6 shows an incident and reflected rays on multi-layers with two different refractive index materials alternatively stacked together with quarter wave thicknesses (wavelength divided by 4 refractive index). For high reflection coatings, a higher refractive index material should be coated at the top. A first reflected ray has a π phase difference with respect to the incident ray due to the fact that a wave has a π phase shift when it reflects against a material with higher refractive index than the material that it is propagating. A second reflected ray at the interface between first and second layers also has π phase difference with respect to the incident ray due to the optical path difference (OPD) of a half wavelength. If a ray reflects from a material that has lower refractive index than

the material that the ray is travelling in, there will not be a π phase shift. A third reflected ray that reflects between second and third layers has a phase difference of a 3π. The OPD of a wavelength causes a 2π phase shift while the other additional π phase shift comes from the ray reflecting off from the dense medium. This structure is repeatedly stacked so that all reflected rays constructively interfere with each other to increase reflectivity.

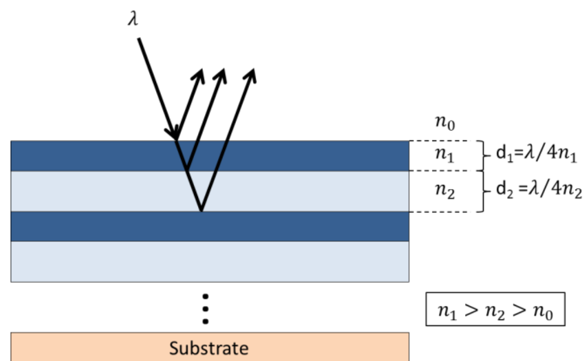

Figure 6 Diagram of Multi-layers for high reflection

Figure 7 shows a dependence of the reflectivity of a multilayer stack of Si/Mo layer pairs at a wavelength of 13.5 nm on the number of layer pairs used [25]. The top material is Si (n=1.03 [26], d=3.277 nm) and the bottom material is Mo (n=0.93 [26], d=3.63 nm) with different number of periods. As the periodic stack number increases, the reflectivity of the coating increases up to a certain level where it saturates due to penetration limit of the radiations.

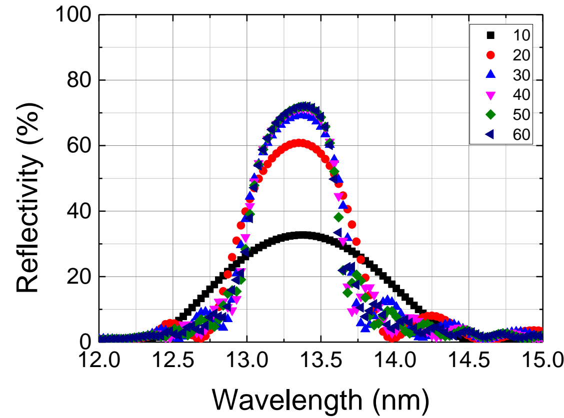

Figure 7 Reflectivity of Si/Mo multilayer with stack numbers at normal incidence [25]

1.3 Refractive Optics

Even though refractive indices in materials for X-rays are close to unity [15], they are not exactly 1. Compound refractive lenses (CRLs) are used for focusing hard X-rays suggested in 1996 by Snigirev *et al*. [27]. A real part of refractive indices for X-rays is expressed as

$$n = 1 - \delta, \tag{3}$$

where δ is a small positive decrement on the order of 10^{-5} to 10^{-6} [28]. A refractive indices for visible light are greater than one so that a shape of positive lenses for focusing is typically bi-convex. In contrary, focusing lenses for X-rays are shaped as bi-concave since the refractive index is smaller than one. Materials for CRLs are very limited due to the absorption. Suitable candidates are Lithium, Beryllium, Carbon, and Aluminum.

For a thin lens, a focal length is determined as

$$\mathrm{f} = \frac{R}{2\delta} \ , \qquad (4)$$

where R is a radius of concave surfaces shown in Figure 8.

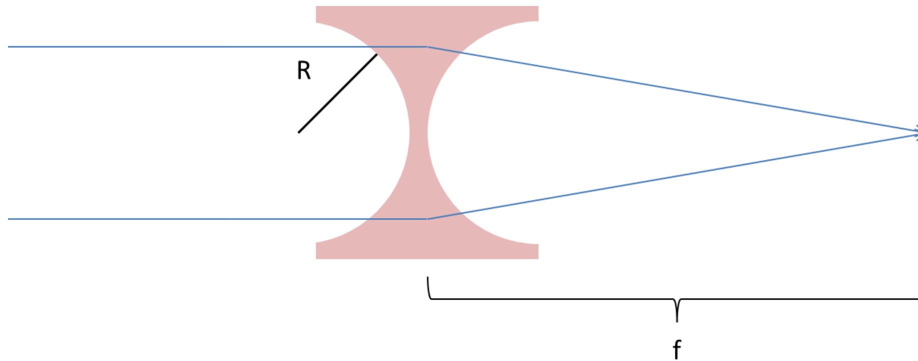

Figure 8 Single CRL

1.4 Diffractive Optics

Diffractive gratings can be used as imaging optics for X-ray microscopy. The gratings indicate periodic structure with different spacing. They follow the grating equation:

$$m\lambda = d(\sin\alpha + \sin\beta), \qquad (5)$$

where α and β are incident and diffractive angles, respectively, d is a groove spacing, and m is a grating order. According to the Rayleigh criterion, a resolution of the planar grating shown in Figure 9 is

$$R = mN, \qquad (6)$$

where N is the number of illuminated grooves [29].

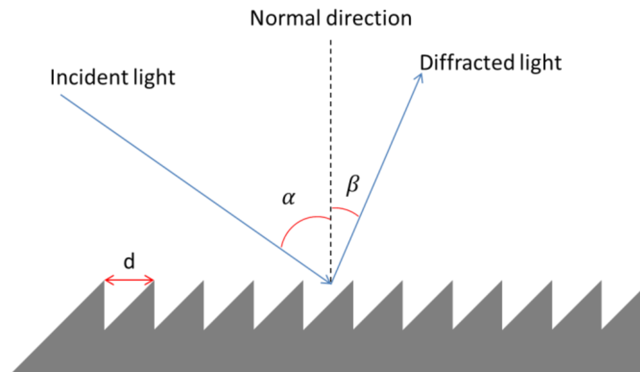

Figure 9 Planar diffraction grating

A concave diffraction grating has an advantage that one less optics can be used in the short wavelength region where light is lost at every optical surface in the system. Rowland circle is defined as a circle having its diameter equal to the radius of the concave grating [30]. If a source is on the circumference of the Rowland circle, diffracted beams are focused on the Rowland circle as shown in Figure 10. Nevertheless, due to the curved image plane, it is tough to observe signals in one direction with a flat detector device. In 1980, an aberration-corrected concave grating was introduced [31] to detect diffracted radiations with a flat field shown in Figure 11 [32].

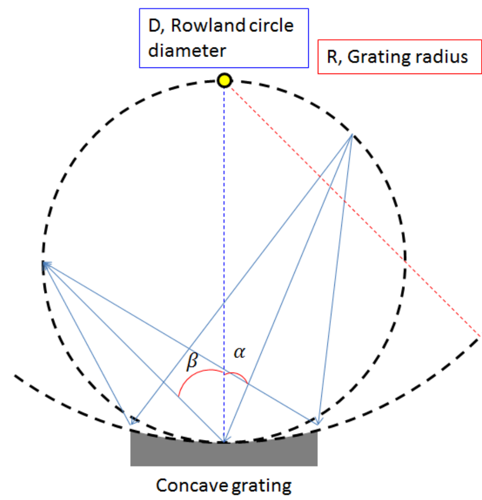

Figure 10 Concave diffraction grating

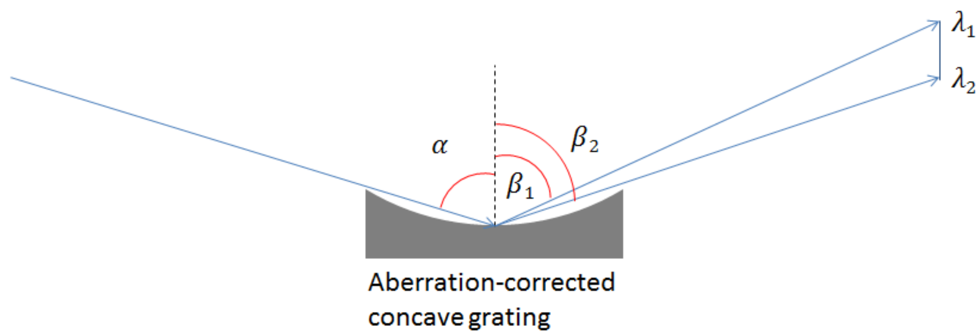

Figure 11 Aberration-corrected concave grating

Another type of diffractive X-ray imaging system is a Fresnel Zone plate (FZP) [33], which is a circular phase grating. It consists of co-axial opaque and transparent rings with radii,

$$r_n^2 = n\lambda f + \frac{n^2\lambda^2}{4} \approx n\lambda f, \qquad (7)$$

where n is an integer indicating transparent zone edges, f is a focal length, which is a distance between a plate and an image plane. The equation (7) is defined by its geometry based on the Pythagorean theory.

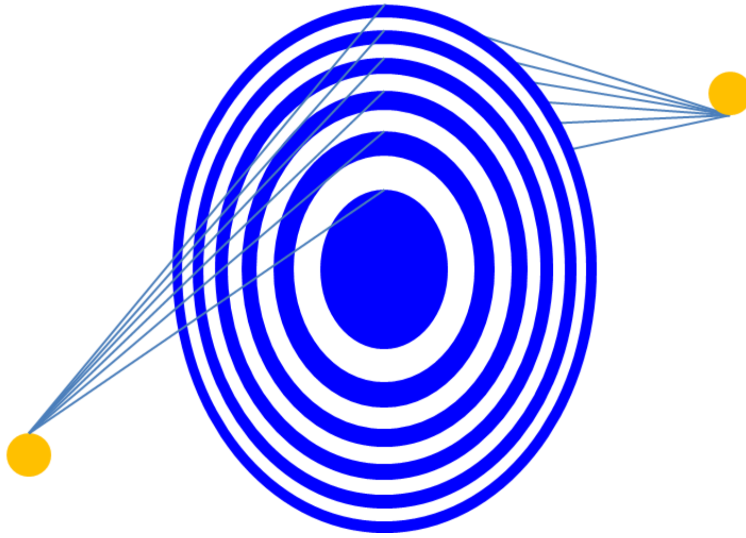

Figure 12 Diffracting Fresnel Zone plate

A width of the outer transparent zone decides a property of the FZP given by

$$\Delta r = r_{n_{max}} - r_{n_{max}-1}. \quad (8)$$

Using this parameter, following parameters can be approximated:

$$D \cong 4n\Delta r, \quad (9)$$

$$f \cong \frac{4n(\Delta r)^2}{\lambda}, \quad (10)$$

$$NA = \frac{D}{2f} \cong \frac{\lambda}{2\Delta r}, \tag{11}$$

$$Depth\ of\ field\ \Delta z = \pm\frac{\lambda}{2(NA)^2} \cong \pm\frac{2(\Delta r)^2}{\lambda}, \tag{12}$$

$$\frac{\Delta\lambda}{\lambda} \leq \frac{1}{n_{max}}. \tag{13}$$

A typical wavelength for FZPs is about 10 nm with n_{max} of 100 or 10000. General efficiencies are about 25 % and 10 % for 0th and 1st order diffractions, respectively [15, 24].

CHAPTER 2: OPTICAL SYSTEM

2.1 Schwarzschild Objective Ray Tracing

The ray tracing was performed with the CODE V that is a commercial software for optical designs. The source was considered as a point source emitting photons to every radial direction. The mirror sizes were set as 2 and 0.5 inches for the primary and the secondary mirrors, respectively, since they are commercially-available sizes. In addition to the availability, it meets the maximum acceptable central obstruction (CO) ratio in telescope engineering given as

$$CO_{max} = \frac{d_{max}}{D} \sim \sqrt{1 - \sqrt{e^{-(2\pi\omega)^2}}}, \qquad (14)$$

where D and d are the diameters of the primary and secondary mirrors, respectively, and ω is the root-mean-square (RMS) wavefront error throughout an aperture. Conventionally, ω value of 0.0752 is used as "diffraction-limited" corresponding to the Strehl ratio of 0.8. The maximum acceptable CO from the equation (14) is 32 %. The Strehl ratio was introduced by Karl Strehl [34], defined as the ratio of intensity from an actual wavefront to one from a reference wavefront in a Gaussian image plane. An approximated form of the Strehl ratio in a circular aperture was suggested by Mahajan [35],

$$S \cong e^{-(2\pi\omega)^2}, \qquad (15)$$

which is compatible with the peak intensity obstructed by the secondary mirror,

$$S \cong (1 - CO^2)^2. \qquad (16)$$

The primary mirror should have a hole at the center, allowing photons to pass through. Considering the experimental setup, the total track should be between 600 and 641.35 mm to avoid interrupting other equipment. The length between the source and the secondary mirror should be longer than 150 mm to reduce an obstructed NA by the secondary mirror and to protect the optical system from debris coming from the source. The ideal magnification is determined by a pixel size of a detector and an Airy disk radius,

$$\mathrm{M} = (2 \times pixel\ size) \times \frac{NA_{object}}{0.61\ \lambda} \tag{17}$$

, which is called the matching resolution. The Airy disk radius multiplied by the magnification is the resolvable minimum length determined by the optical system. The pixel size time 2 is the minimum resolvable length by the detector. If the two lengths are same, the best spatial resolution can be reached. If different, the lower resolution limits the spatial resolution. For instance, the magnification should be larger than 27.98 at 150 nm wavelength with a NA of 0.1, and a pixel size of 12.8 μm.

With above constraints, one solution was found with off-the shelf mirror substrates. The optical system specification is listed in Table 1. The spot diagrams of different object heights are shown in Figure 13. According to Table 1, the biggest aberration is coma. The coma is dependent on an object height so that the on-axis spot diagram does not show the coma aberration. In contrary, the image with 100 μm object height has the coma shape aberration. However, the aberrations are smaller than the Airy disk so that this optical system is diffraction-limited.

Table 1 Specification of Schwarzschild objective

Mirror diameter and radii	Primary: 50.8 mm and -206.6 mm (Concave) Secondary: 12.7 mm and 103 mm (Convex)
Distances	From source to primary: 291.4 mm From primary to secondary: 113.8 mm From secondary to image: 457.4 mm
NA or F-number	Objective: 0.075559 or 6.62 Image: 0.013922 or 35.91
Magnification	5.43 (Real)
Aberrations	Spherical: 0.000249 Coma: -0.000739 Tangential astigmatism: -0.000035 Sagittal astigmatism: -0.000025 Field curvature: -0.00002 Distortion: 0
Central obstruction	10.41 mm (40.98 %)
CCD pixel size	12.8 μm × 12.8 μm
Number of pixels	1024 × 1024

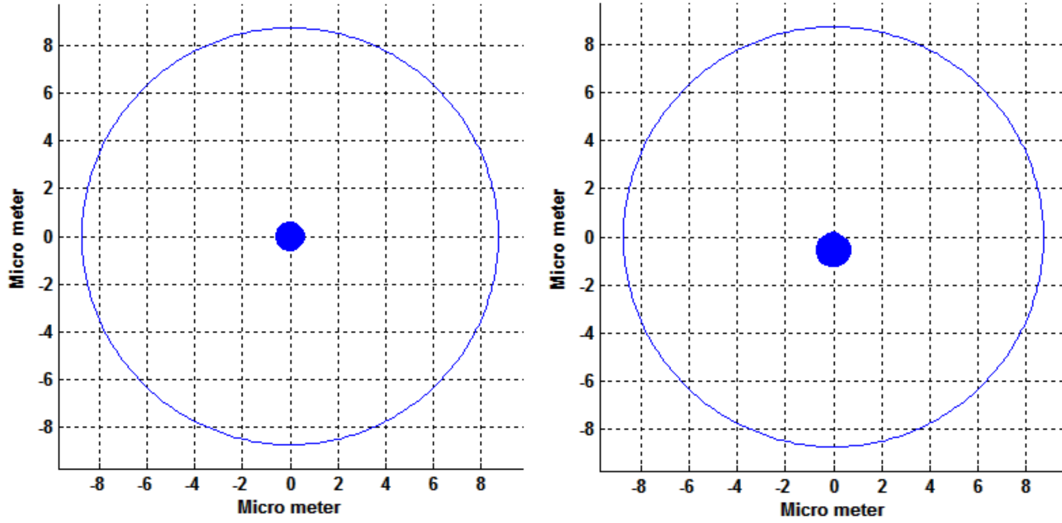

Figure 13 Spot diagrams with Airy disks in the image plane with different object height, on-axis (left) and 100 μm from the axis (right)

An optical system resolution is expressed in several ways. A modulation transfer function (MFT) is typically used for a spatial resolution related to image contrasts. The contrast is defined as

$$C(\xi) = \frac{I_{max} - I_{min}}{I_{max} + I_{min}}, \qquad (18)$$

where ξ is a spatial frequency and the contrast is between 0 and 1. A MTF is an optical system property that shows how well it transfers the contrast of an object to an image plane through the system represented by

$$MTF(\xi) = \frac{C_{image}(\xi)}{C_{object}(\xi)}, \qquad (19)$$

where each subscript indicates image and object contrasts, respectively. A MTF is also determined by the diffraction theory [36]. A MTF curve shows a linear behavior from low frequency given as

$$\xi_{linear} = \frac{NA_{image}}{0.61\,\lambda}, \tag{20}$$

and a limiting frequency is

$$\xi_{limit} = \frac{NA_{image}}{0.5\,\lambda}. \tag{21}$$

Figure 14 shows several MTF curves on the Schwarzschild objective. The black dash line is the diffraction-limited MTF curve and the red X-line is the actual MTF curve of the system. The red dash line is the diffraction-limited MTF curve without any obstruction. The pink dash line is the MTF curve of the obstruction, so that the optical system MTF curve is placed between those lines. In higher frequency regions, the optical system curve is higher than non-obstructed one because MTF is a convolution of two apertures: due to the obstructed area, the total area with the obstruction is smaller than one without the obstruction so that the ratio of overlapping areas to opened aperture areas is larger than the unobstructed case.

In addition to the aberration and the obstruction effects on MTF, a detector MTF should be considered. The total system MTF is given by

$$\mathrm{MTF}_{total} = \frac{\sin(p\xi\pi)}{p\xi\pi} \times \mathrm{MTF}_{optical\ system}, \tag{22}$$

where p is the pixel size [37]. The blue dash line is the pixel MTF with 12.8 μm pixel size with 5.43 magnification and the green star line is the total system MTF curve. An expected object size is about 100 μm and it corresponds to a 5 lp/mm that has a 90 % modulation.

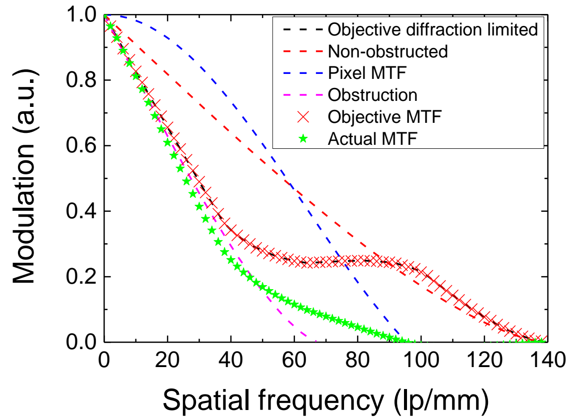

Figure 14 Modulation transfer function (MTF)

2.2 Spider Diffractions in Schwarzschild

A Schwarzschild telescope has a diffraction problem caused by its second mirror holder called spiders, shown in Figure 15. The diffraction is related to the degree of coherence that is proportional to the Bessel function of first kind with first order for the circular source. The degree of coherence is given by

$$\gamma \sim J_1\left(\frac{\pi D l}{\lambda z}\right), \tag{23}$$

where D is a diameter of a source, l is the aperture size, and z is the distance between the source and the aperture. The degree of coherence reduces with increasing the argument and finally becomes zero if the argument is larger than 1.22π.

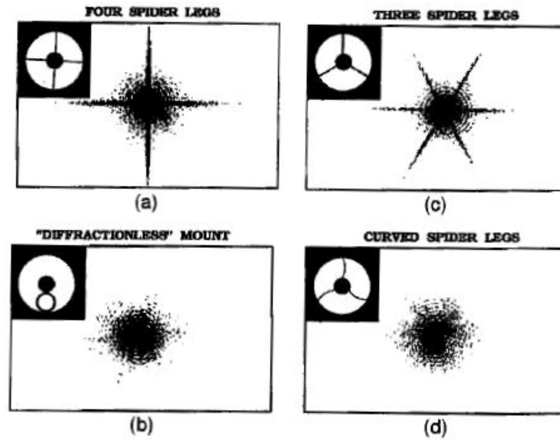

Figure 15 Diffraction effects of secondary mirror spiders on image quality [38]

Figure 16 shows diffraction patterns with different source diameters with l = 1 mm, z =11.48 cm, and λ = 550 nm, so that the arguments of (a), (b), and (c) are 0.158 π, 0.792 π, and 1.584 π, respectively. Diffraction patterns are observed in (a) and become weak but still existing in (b). They have the lower argument than 1.22 π. Diffraction patterns disappear in (c) because the argument is larger than 1.22 π.

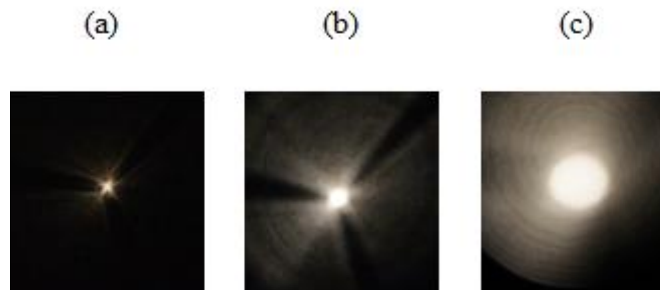

Figure 16 Images of different pinhole sizes D = (a) 10 μm, (b) 50 μm, and (c) 100 μm

By using the same method, the 42 μm at the smallest diameter that will be plasma size can be observed without diffraction patterns, with the parameters: $l = 1$ mm, $z = 0.177$ m, and $\lambda = 194$ nm. However, the shadow of the spiders could be problematic. Therefore, the secondary mirror will be attached to an MgF_2 window to avoid this problem.

2.3 Mirror Coatings

The Drude model explains that an incident photon with higher frequency than a plasma frequency of a metal transmits the interface. In contrary, lower frequency input photon usually reflects against the metal-air interface. Therefore, high plasma frequency metal is desirable for the broadband mirrors.

For broadband metallic mirrors, commercially available Aluminum (Al) and Magnesium Fluoride (MgF_2) coating was used. Al has the plasma frequency of $v_p = 3.57 \times 10^{15}/s$ [39], which corresponds to the wavelength of 84 nm. Therefore, Al reflects longer wavelength than 84 nm, but Al_2O_3 can be spontaneously deposited on an Al film, which absorbs shorter wavelength than 200 nm. To avoid the Al_2O_3 deposition, other materials should be coated on top of Al such as MgF_2 that has a wide transmittance range from about 120 to 7000 nm shown in Figure 17. Figure 18 shows the reflectivity of commercially-available Al/MgF_2 coating.

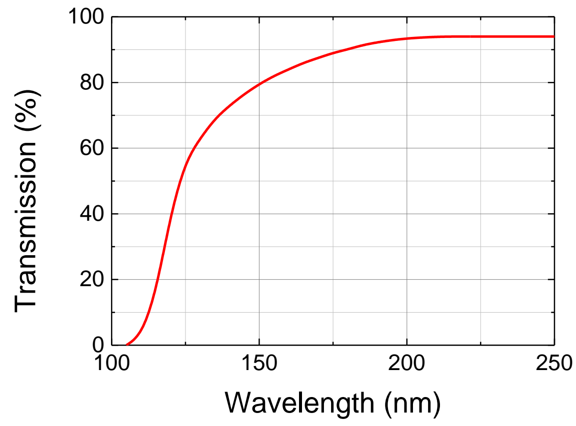

Figure 17 Transmission of MgF_2 window

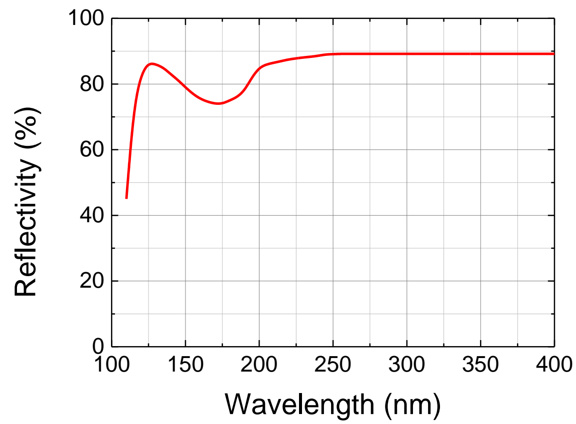

Figure 18 Reflectivity of Al/MgF_2 coating

2.4 Optical Bandpass Filter

To observe plasma within certain ranges of wavelengths, an optical bandpass filter is needed. Optical filters play a role in selectively transmit or block a certain range of wavelengths. Figure 19 shows commercially-available filter transmissions at 172 and 194 nm as peak wavelengths. A full widths at half maximums (FWHMs) are 23.5 and 13.37 nm, respectively.

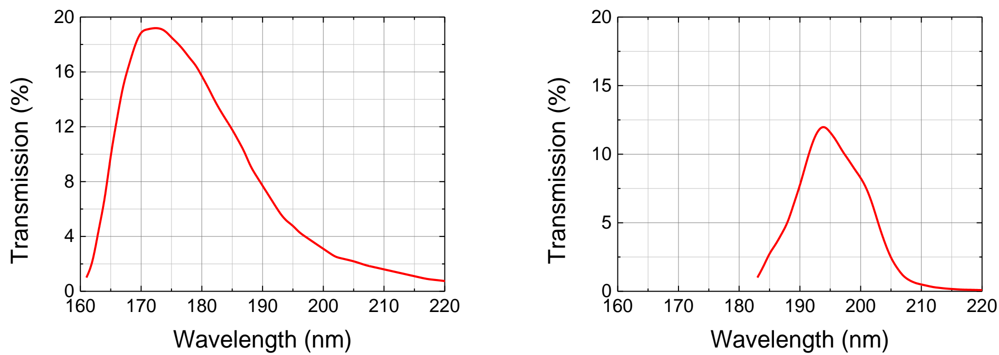

Figure 19 Transmissions of bandpass filters

CHAPTER 3: EXPERIMENTAL APPARATUS

3.1 Intensified charge-coupled devices

A charge-coupled device (CCD) has been used as an image sensor. PI MAX 3, an intensified charge-coupled device (ICCD) that can intensify signals by using a Microchannel plate (MCP) is used. The ICCD is suitable for a high speed operation due to the fact that it can intensify weak input signals with a narrow camera shutter bandwidth.

PI MAX 3 consists of an input window, a photocathode, an MCP, a fluorescent screen, a fiber-optic bundle, and a CCD array as it is shown in Figure 20. There are electrical connections between components in order to apply voltages to intensify signals. Photons are incident onto the photocathode that converts photons to electrons. When the gate turns on, the negative voltage is applied on the photocathode side and the positive voltage is applied on the fluorescent screen side to accelerate electrons toward the MCP. The MCP will generate extra electrons to intensify signals. The electrons intensified by MCP hit the fluorescent screen that emits photons. The fiber-optic bundle collects the photons into the CCD array. The MCP gain can be regulated from 1 to 100 that match 2.08 to 208 times of original signals.

Figure 21 presents the quantum efficiency of ICCD. The manufacture provides the efficiency curve cut off at 200 nm and the input window is made of UV fused silica that transmits 160 nm at shortest. The efficiency curve was obtained by matching the transmittance of UV fused silica and the efficiency curve.

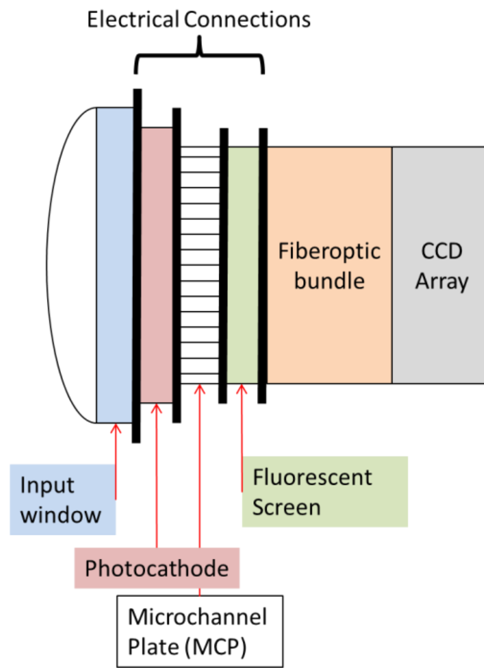

Figure 20 Schematic diagram of ICCD

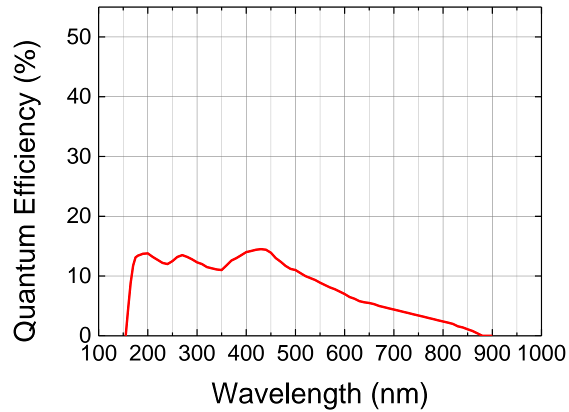

Figure 21 Quantum efficiency of the ICCD

3.2 Photon budgets

It is important to estimate how many photons are coming from the source through an experimental setup. According to the expectation before experiments, it can be found whether potential system can measure signals or not. All experimental errors cannot be expected, so that the photon budget should be considered in a worst case.

Figure 22 shows Sn and Zn spectral irradiance measured by the Maya spectrometer at 800 mm from the source. 0.001 μW/(cm^2 nm) was used for an under-estimation. The primary mirror of Schwarzschild objective should be located at 291 mm, where the spectral irradiance is 0.0076 μW/(cm^2 nm). It is assumed that a wavelength bandwidth, $\Delta\lambda$, is 1 nm.

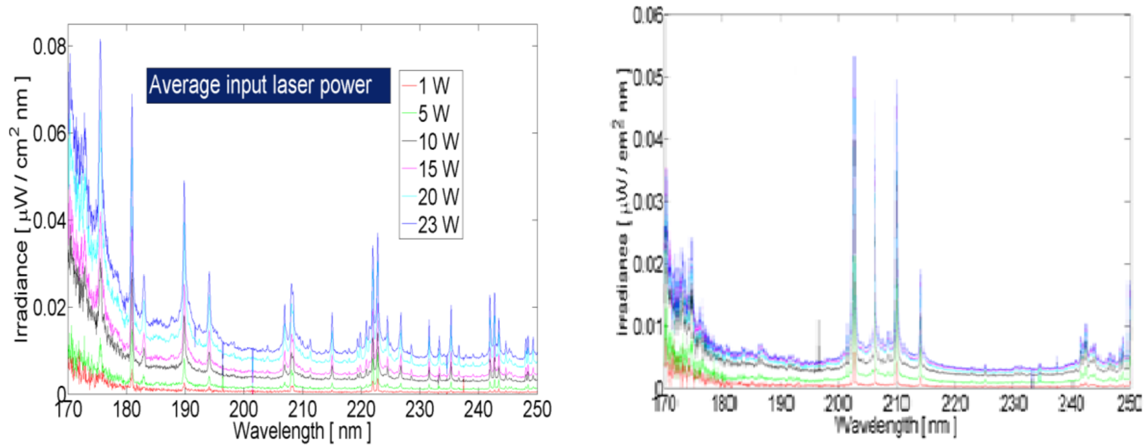

Figure 22 Sn and Zn spectral irradiance with different input laser powers at 0.8 m

Figure 23 shows total calculated efficiencies through the system regarding the mirror reflectivity, the transmission of the filter, the three MgF_2 windows and the quantum efficiency of

the ICCD. An integration of the whole signals indicates the total number of electrons being detected on the total CCD array. The number of electrons should be divided by the number of pixels (1024 × 1024) and the repetition rate of the input laser (100 Hz), which are 279.25 and 147.17 e/pixel/s, respectively. This ICCD has a dark charge of 3.44 e/pixel/s, which is about 80 and 40 times lower compared to the input signals. Therefore, this system can measure a laser induced plasma at 172 and 194 nm wavelengths from Zn and Sn.

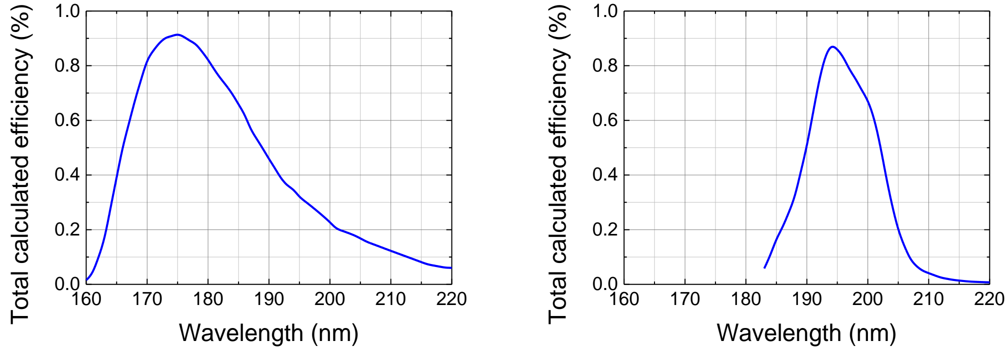

Figure 23 Total calculated efficiency of the whole system

3.3 Timing

A laser pulse breaks bondages between atoms, ions, or molecules. Plasma is generated by deflecting electrons (Bremsstrahlung, continuum radiation), recombining electrons with ions. A transition between atoms, ions, and molecules generates line emissions [40]. Emissions shorter than 400 nm wavelengths disappear after 250 ns from a generation of plasma with solid targets. [41]. The shorter wavelength emission disappears faster than the longer wavelength emission. For

example, an emission at 282 nm decays to 10 % of its peak intensity after 60 ns and another emission at 360 nm takes about 140 ns.

It is required to synchronize the laser system and the ICCD. The laser system is controlled by a delay generator that resolves 1ps at most. The laser, the delay generator, and the ICCD should be connected to each other for synchronization shown in Figure 24. The repetition rate of the laser is 100 Hz. A time difference between the flash lamp and Q-switch is 198 µs. To find the time that the laser pulse arrives at the target position, a fast photodiode was used externally triggered by the delay generator with cables that has a known delay time. The time between Q-switch turning on and the laser pulse arrival at the target position is 299.35 ± 4 ns and the ICCD gate delay 55.71 ns is shown in Figure 25. Therefore, the ICCD delay should be 243.64 ns. Regarding the time delay that the pulse reflects and travels to ICCD, the final ICCD delay becomes 245.76 ns because the total distance throughout the optical system is 635 mm (2.12 ns).

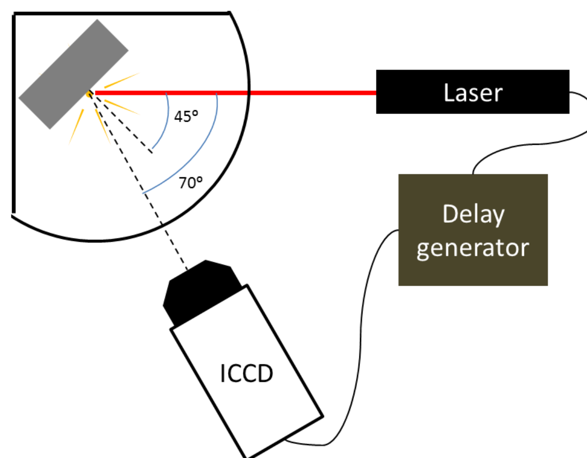

Figure 24 Schematic of experimental setup

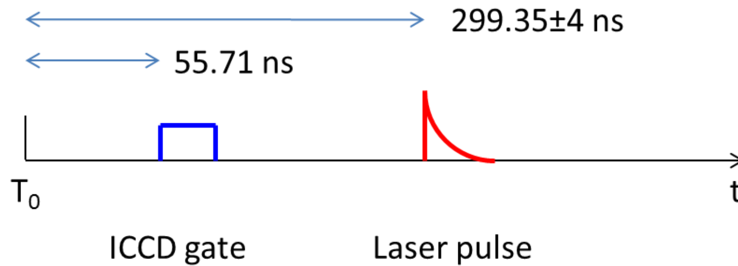

Figure 25 Measured timing diagram

3.4 Degrees of Freedom

To align the optical system, degrees of freedom of optics should be considered because although many degrees of freedom compensate mechanical limitations, it is hard to find a right alignment or takes a long time. In contrary, fewer degrees of freedom may cause a reconstruction of a whole system.

The primary and the secondary mirrors in the Schwarzschild objective have 6-degrees of freedom, 3-axis translations (X, Y, Z), tip-tilts (θX, θY), and a rotation. However, the degrees of freedom should be minimized regarding mechanical limitations. The two spherical mirrors are rotational symmetric, so that the rotation is not needed. X and Y positions are relative to each other, and X and Y movements are removed in the secondary mirror, assuming that a tolerance of the secondary mirror location is less than 0.2 mm. To reduce the secondary mirror position tolerance, a mold was fabricated to glue the secondary mirror onto the MgF_2 window shown in Figure 26. The size of the hole is 0.5 inch + 0.2 mm due to the mirror diameter tolerance. It is found that 0.2

mm tolerance does not affect spot diagrams and an MTF much in the CODE V simulation. Figure 26 shows a picture of the convex mirror glued to the MgF_2 window.

The primary and the secondary mirrors are on the optical rail that restricts the freedom in X and Y directions when the distance between mirrors is adjusted in Z-direction. ICCD is only adjustable in Z-direction. The total experimental setup is shown in Figure 27.

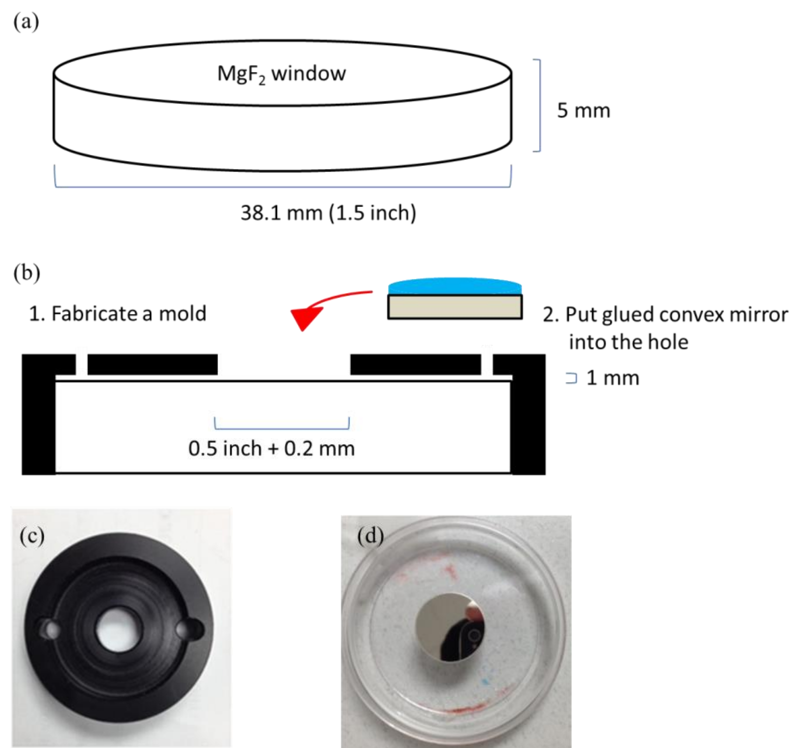

Figure 26 (a) Diagram of MgF_2 dimension, (b) procedure of how to glue the secondary mirror on MgF_2 window, (c) picture of mold, and (d) convex mirror glued to the MgF_2 window

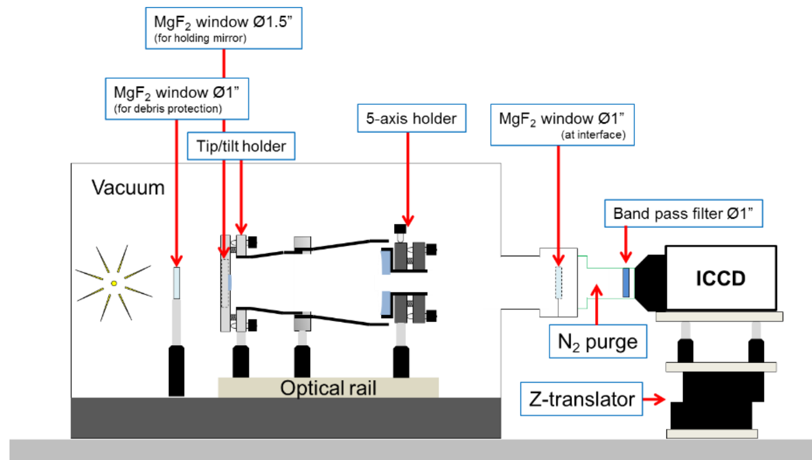

Figure 27 Experimental setup

3.5 Sensitivity of Adjustments

A sensitivity test simulation is performed at 172 nm wavelength (harder than 194 nm to reach for diffraction-limited due to the smaller Airy disk) with different object heights, 0, 50, 100, and 150 µm. The tip/tilt mirror holders use knobs with 100 and 32 threads per inch (TPI) for the primary and the secondary mirrors, respectively. Assuming that the minimum tunable rotation degree for knobs is 1° so that the minimum adjustable mirror tilt degrees are 0.001^{o} and 0.003^{o} for the primary and the secondary mirrors, respectively regarding the knob TPIs and the distance between the knobs and pivots of mounts. Figure 28 shows spot diagrams of 10 degree knob changes for (a) the secondary, (b) the primary tip/tilt and (c) a 0.1 mm variation of the primary mirror in Z-direction. Tip/tilt variations are still within a diffraction-limited quality, which less sensitive than Z-direction variations.

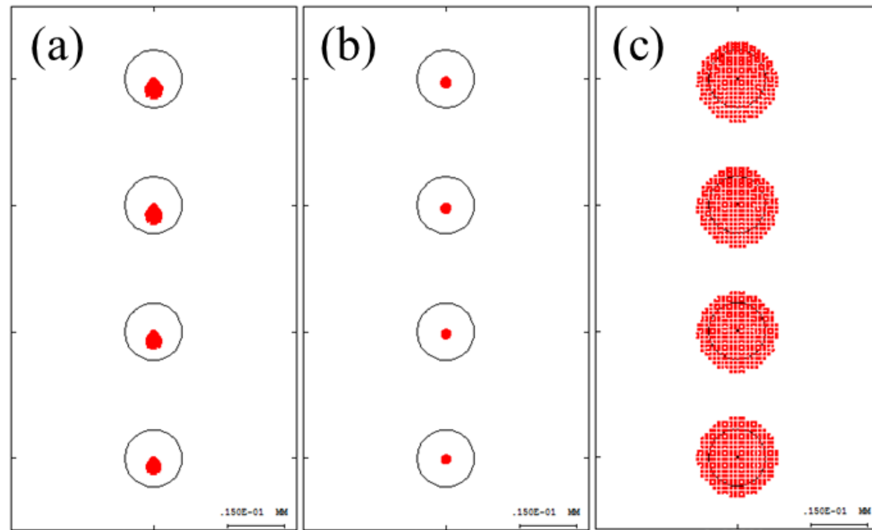

Figure 28 Spot diagrams with 10° rotations of knobs of (a) secondary, (b) primary tip/tilt, and (c) a 0.1 mm distance variation of the primary mirror in Z-direction

According to the sensitivity, the system alignment should be adjusted in Z-direction first. The height of optical axis comes first. The mirrors are on an optical rail, so that the distance between two mirrors should be fixed with right distance. Then, the total rail system should be placed in a suitable position considering the detector position. Finally the angle should be adjusted.

CHAPTER 4: RESULTS

4.1 Imaging System Analysis

Figure 29 shows a resolution chart image by using the optical system and a Deuterium lamp spectrum [42]. The Deuterium lamp that has high intense emissions in the VUV region. Any filters could not be used due to a high signal-to-noise ratio. Considering the spectrum and the efficiencies of the mirrors, the MgF_2 windows, and the CCD, the peak wavelength is expected around 220 nm. The shortest wavelength is about 175 nm. The magnification is obtained by pixel counts. Group 4 (column) -element 2 (row) has a 27.86 μm line width. The average number of pixels covered by one bar is 11.58 pixels that corresponds to a 148.26 μm. The magnification is 5.32 and the simulated magnification was 5.43 in CHAPTER 2. The minimum resolvable bar set is a group 6-element 4 as 13.46 % modulation, which is 90.5 lp/mm (5.52 μm line width). This is higher resolution than the simulated resolution of 64 lp/mm at 10 % modulation, which results from the shorter wavelength light source than 194 nm.

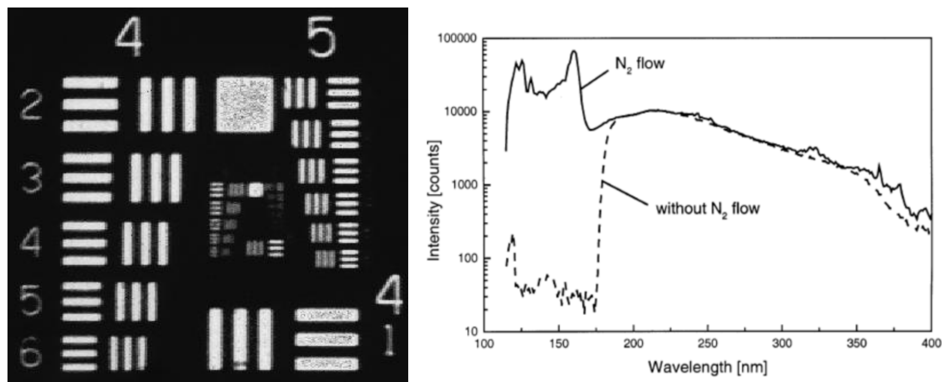

Figure 29 Resolution chart image and Deuterium lamp spectrum [42]

4.2 Plasma Images

An Nd:YAG laser at 1064 nm wavelength in a 100 Hz repetition rate was used with 10 µm radius beam profile. Zinc and Tin metal plates were used on a rotational stage in order for a laser pulse to shoot an undamaged surface by its previous laser pulses. The gate width is 10 ns and the start points are delayed by 10 ns. A plasma image is not taken with the single laser pulse because the laser repetition rate is 100 Hz and the camera has 25 frames per second (FPS). The solid target plasma is stable enough so that similar images can be obtained from different laser pulses. The input laser intensities were from 1.5 to 31×10^{10} W/cm^2 and two filters were used, 172 and 194 nm. Figure 30 through Figure 33 show the plasma images with different laser intensities and different peak wavelengths. In the images, the target is located left and the laser pulses incidents from right.

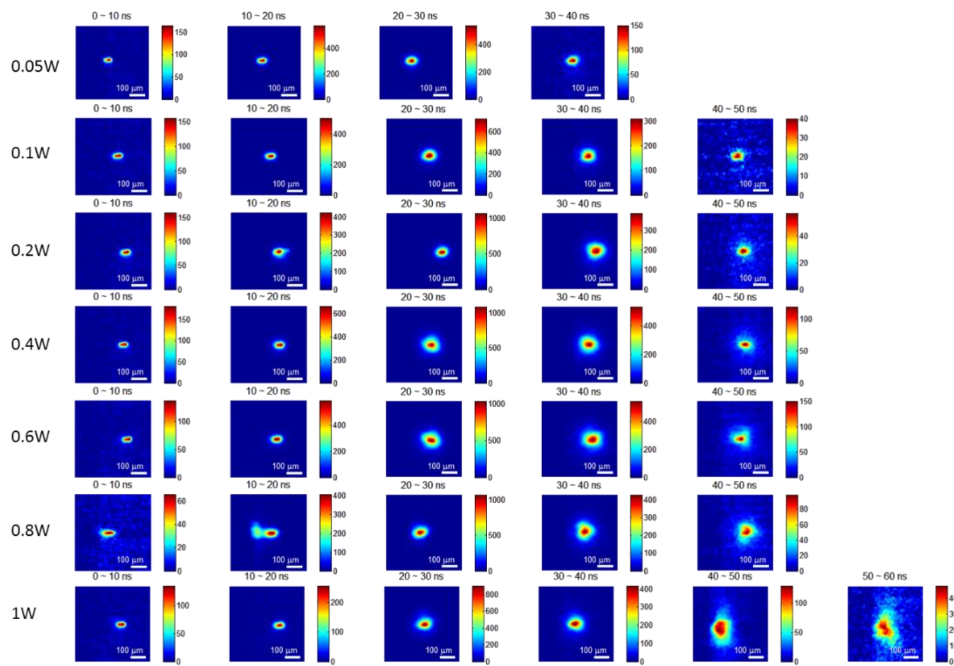

Figure 30 Zn target plasma images with 172 nm filter

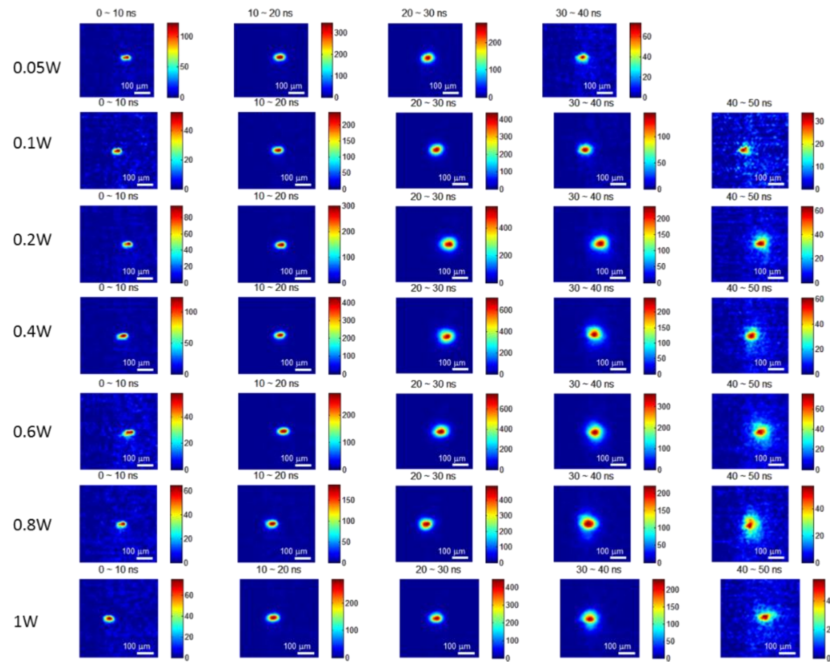

Figure 31 Zn target plasma with 194 nm filter

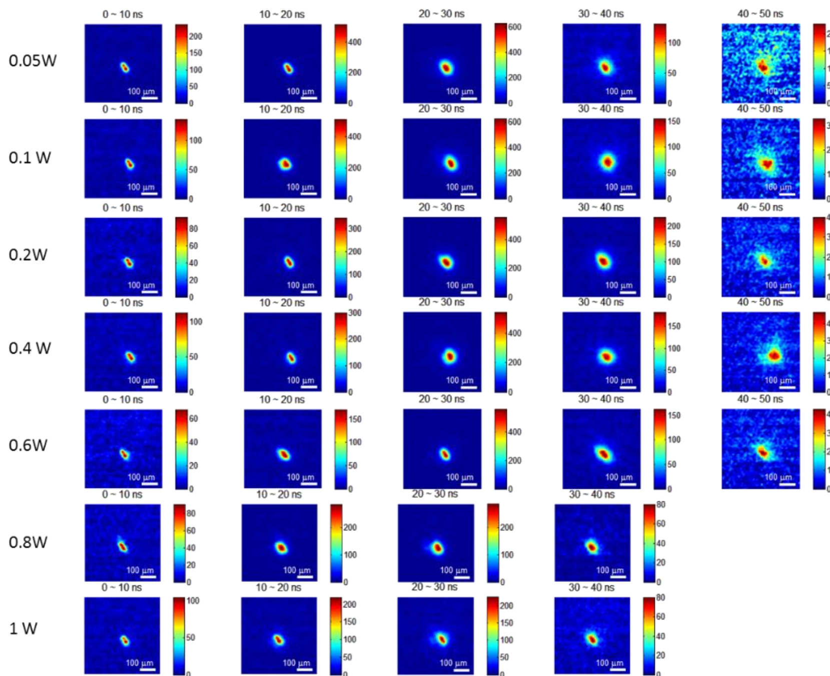

Figure 32 Sn target plasma images with 172 nm filter

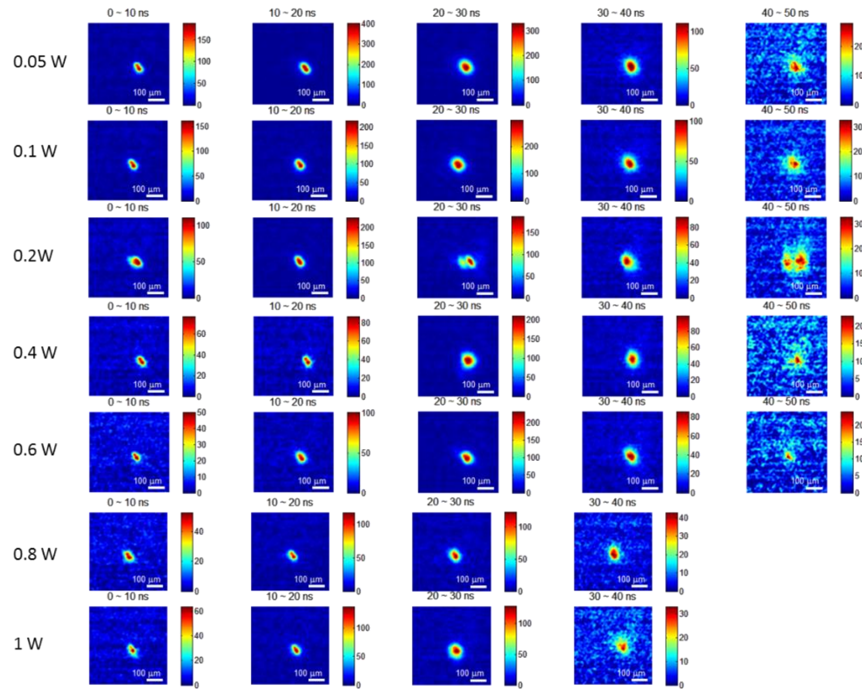

Figure 33 Sn target plasma images with 194 nm filter

4.3 Plasma Dynamics and Input intensity Dependencies

The images shown in the previous section are not showing any big difference between two different filters so that this section shows 172 nm filter data. Figure 34 shows Zn plasmas images and maximum intensity changes in a time domain. Plasma emissions disappear after 60 ns in average. The emissions hit the peak point between 20 – 30 ns.

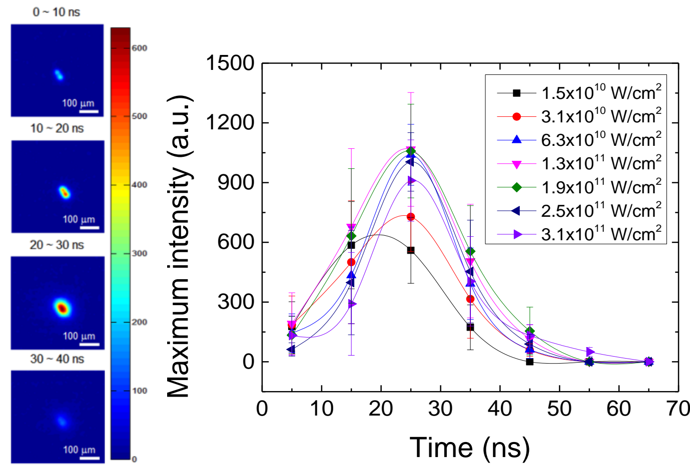

Figure 34 Lowest intensity Zn plasma images in a same scale and transient plasma maximum intensities with different input laser intensities

The diameters of plasmas were determined as lengths above two times of the noise level to get total plasma emission areas. The plasmas reach the biggest size after maximum plasma emissions shown in Figure 35. After 60 ns, the diameters decrease, but this doesn't mean plasmas disappear. An electron density is reduced after 60 ns, there still is low temperature plasma emitting long wavelengths.

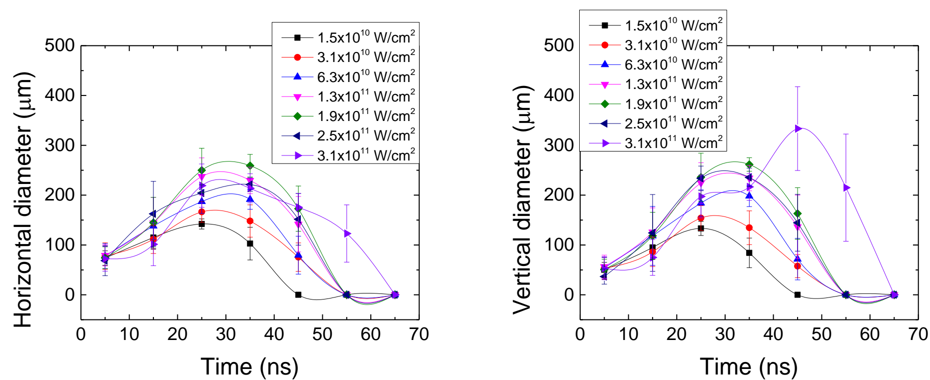

Figure 35 Horizontal and vertical Zn plasma diameters in a time domain

To find out the most efficient laser input intensity, output/input ratios that is the value of maximum plasma intensities divided by the input laser intensities are shown in Figure 36. The output/input ratio is proportional to a conversion efficiency. The efficiency is decreased with increasing input laser intensities. The diameters shown in Figure 36 increase with increasing laser input intensities. The diameters at the most efficient condition is about 100 μm.

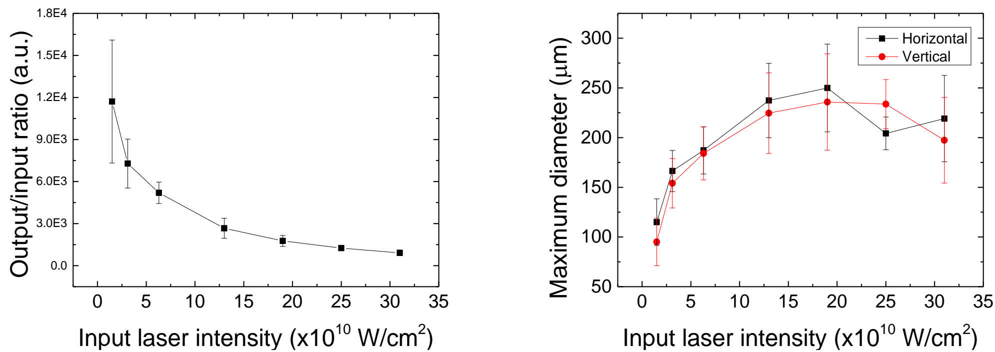

Figure 36 Ouput/input ratio and maximum diameters of Zn plasmas in terms of input laser intensities

Sn plasmas have similar trends in a time domain shown in Figure 37 and Figure 38. The maximum intensities are emitted between 20 – 30 ns and in-band plasmas disappear after 50 ns. One difference from Zn plasmas is the maximum diameters are shown at the maximum intensity time.

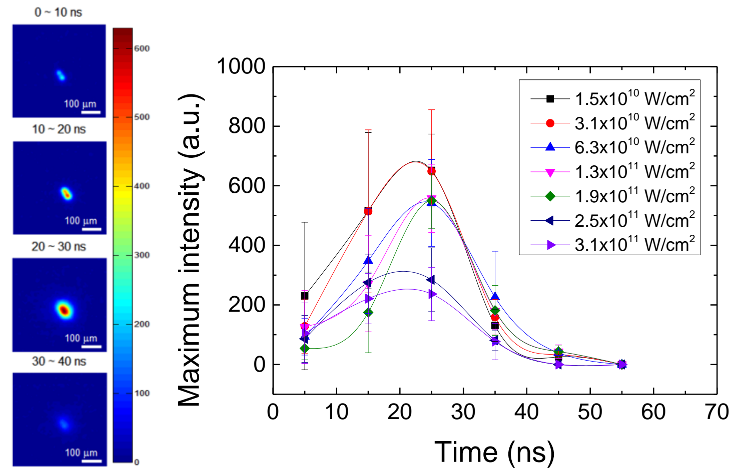

Figure 37 Lowest intensity Sn plasma images in a same scale and transient plasma maximum intensities with different input laser intensities

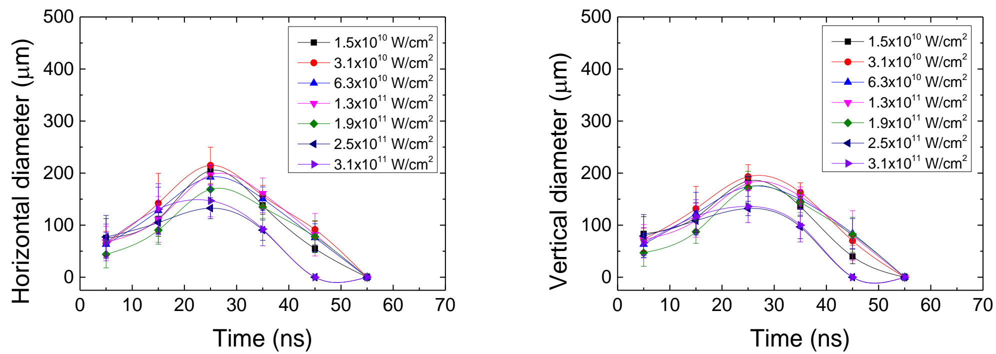

Figure 38 Horizontal and vertical Sn plasma diameters in a time domain

The conversion efficiency also decreases and the diameters decrease with increasing input laser intensities shown in Figure 39. At the most efficient intensity, Sn plasma has about 200 μm diameters. The main difference between Zn and Sn is the slope of horizontal and vertical diameters

that Zn has positive slopes and Sn has negative slopes. In both Zn and Sn plasma cases, the ratios of emissions to input powers are reduced with increasing input laser powers. The best efficiency can be achieved at lower input laser intensities. Therefore, the experiments with lower input laser powers should be conducted to find the most efficient laser powers.

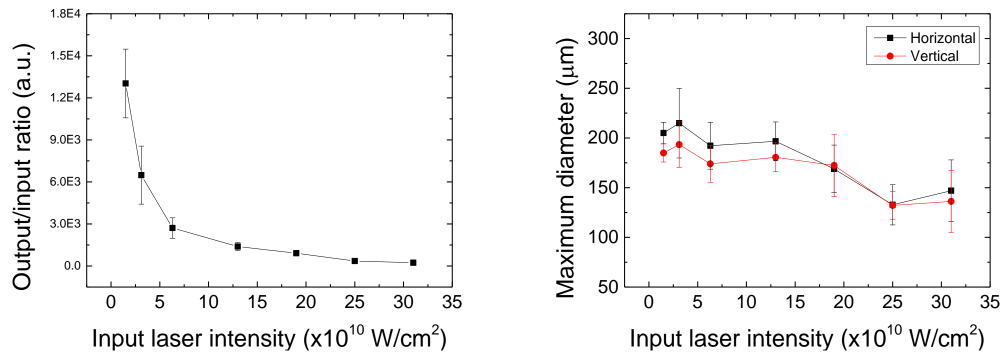

Figure 39 Ouput/input ratio and maximum diameters of Sn plasmas in terms of input laser intensities

CHAPTER 5: CONCLUSIONS

Several types of optics for short wavelengths were reviewed. The time-resolved imaging system was demonstrated by using a Schwarzschild objective with the Al/MgF_2 coating and the ICCD to investigate the Zn and Sn laser-produced plasmas. The 172 and 194 nm filters were applied. The spatial resolution is 5.52 μm at 11 % modulation with a Deuterium lamp. The simulated resolution t is limited by the pixel sizes and the secondary mirror size. Thus, the spatial resolution can be improved by increasing the magnification and by using a smaller secondary mirror. The other CCD that is sensitive in shorter wavelength regions can allow this apparatus to operate at shorter wavelengths with different bandpass filters down to 120 nm wavelength with suitable scintillators. The images show the plasma dynamics and sizes. Lower laser input intensity experiments are required for the most efficient plasma generations.

LIST OF REFERENCES

[1] W. C. Röntgen, "Ueber eine neue Art von Strahlen," *Annalen der Physik,* vol. 64, pp. 1-37, 1898.

[2] W. Friedrich, P. Knipping, M. Laue, "Interferenzerscheinungen bei Röntgenstrahlen," *Annalen der Physik,* vol. 346, no. 10, pp. 971-988, 1913.

[3] William Henry Bragg, William Lawrence Bragg, X-ray and Crystal Structure, Bell, 1915.

[4] M. Richardson, Chapter 3 EUV Sources in Extreme Ultraviolet Lithography edited by Banqui Wu and Ajay Kumar, New York: McGraw-Hill, 2009.

[5] K. Takenoshita, "Debris characterization and mitigation of croplet laser plasma sources for EUV lithography," University of Central Florida, Orlando, 2006.

[6] Martin Richardson, C.-S. Koay, K. Takenoshita, C. Keyser, M. Al-Rabban, "High conversion efficiency mass-limited Sn-based laser plasma source for extreme ultraviolet lithography," *Journal of Vacuum Science and Techonology B,* vol. 22, no. 2, p. 785, 2004.

[7] Martin Richardson, David Torres, Chris DePriest, Feng Jin, Gregory Shimkaveg, "Mass-limited, debris-free laser-plasma EUV source," *Optics Communications,* vol. 145, no. 1-6, pp. 109-112, 1998.

[8] M. Richardson, "EUV, XUV, and X-ray wavelength sources created from laser plasma produced from liquid metal solutions, and nano-size particles in solutions". United States of America Patent US6865255 B2, 8 March 2005.

[9] F. Jin, M. Richardson, G. Shimkaveg, D. Torres, "Characterization of a laser plasma water droplet EUV source," in *SPIE*, 1995.

[10] C. Keyser, G. Schriever, M. Richardson, E. Turcu, "Studies of high-repetition-rate laser plasma EUV sources from droplet targets," *Applied Physics A,* vol. 77, no. 2, pp. 217-221, 2003.

[11] Kazutoshi Takenoshita, Chiew-Seng Koay, Somsak Teerawattansook, Martin Richardson, Vivek Bakshi, "Debris characterization and mitigation from microscopic laser-plasma tin-doped droplet EUV sources," in *SPIE*, 2005.

[12] M. Richardson, "EUV, XUV, and X-Ray wavelength sources created from laser plasma produced from liquid metal solutions". United States of America Patent US6831963 B2, 14 December 2004.

[13] Arindam Mallik, Wim Vansumere, Julien Ryckaert, Abdelkarim Mercha, Naoto Horiguchi, Steven Demuynck , Jürgen Bömmels, Tokei Zsolt, Geert Vandenberghe, Kurt Ronse, Aaron Thean, Diederik Verkest, Hans Lebon, An Steegen, "The need for EUV lithography at advanced technology for sustainable wafer cost," in *SPIE*, 2013.

[14] S. P. D. S.-H. H. Richard W. Solarz, "Optical imaging system with laser droplet plasma illuminator". United States of America Patent US8575576 B2, 5 November 2013.

[15] D. T. Attwood, Soft X-rays and Extreme Ultraviolet Ratiation: Principles and Applications, Cambridge ; New York : Cambridge University Press, 2000.

[16] C. A. Roobottom, G. Mitchell, G. Morgan-Hughes, "Radiation-reduction strategies in cardiac computed tomographic angiography," *Clinical Radiology,* vol. 65, no. 11, pp. 859-867, 2010.

[17] E. Hecht, Optics, Addison-Wesley Longman, Incorporated, 2001.

[18] PAUL KIRKPATRICK, A. V. BAEZ, "Formation of Optical Images by X-Rays," *Journal of the Optical Society of America,* vol. 38, no. 9, pp. 766-774, 1948.

[19] H. Wolter, "Spiegelsysteme streifenden Einfalls als abbildende Optiken für Röntgenstrahlen," *Annalen der Physik,* vol. 445, no. 1-2, pp. 94-114, 1952.

[20] M. Montel, "X-ray microscopy with catamegonic roof mirrors," *Academic Press,* pp. 177-185, 1957.

[21] K. Schwarzschild, Untersuchungen zur geometrischen Optik, Astronomische Mitteilungen der Königlichen Sternwarte zu Göttingen, 1905.

[22] Igor A. Artioukov, Kirill M. Krymski, "Schwarzschild objective for soft x-rays," *SPIE Optical Engineering,* vol. 39, no. 8, pp. 2163 - 2170, 2000.

[23] Reiner Salzer, Heinz W. Siesler, Infrared and Raman Spectroscopic Imaging, Wiley-VCH, 2009.

[24] S. A. George, "Spectroscopic studies of laser plasmas for EUV sources," University of Central Florida, Orlando, 2007.

[25] E. Gullikson, "Multilayer Reflectivity," CXRO, [Online]. Available: http://henke.lbl.gov/optical_constants/multi2.html.

[26] E. D. Palik, Handbook of Optical Constants of Solids, Boston: Academic Press, 1985.

[27] A. Snigirev, V. Kohn, I. Snigireva, B. Lengeler, "A compound refractive lens for focusing high-energy X-rays," *Nature,* vol. 384, no. 7, pp. 49-51, 1996.

[28] K. Young, "Focusing optics for X-ray applications," Graduate College of the Illinoise Institute of Technology, 2005.

[29] R. D. Kamtaprasad, "Laser plasma radiation studies for droplet sources in the extreme ultraviolet," University of Central Florida, 2010.

[30] H.-J. Kunze, Introduction of Plasma Spectroscopy, Springer, 2012.

[31] Tatsuo Harada,Toshiaki Kita, "Mechanically ruled aberration-corrected concave gratings," *Applied Optics,* vol. 19, no. 23, pp. 3987-3993, 1980.

[32] J. M. Szilagyi, "Extreme ultraviolet spectral streak camera," University of Central Florida, 2010.

[33] A. G. Michette, Optical systems for soft X rays, New York: Plenum Press, 1986.

[34] K. Strehl, "Aplanatische und fehlerhafte Abbildung im Fernrohr," *Zeitschrift für Instrumentenkunde,* vol. 15, pp. 362-370, 1895.

[35] V. N. Mahajan, "Strehl ratio for primary aberrations in terms of their aberration variance," *Journal of the Optical Society of America,* vol. 73, no. 6, pp. 860-861, 1983.

[36] J. W. Goodman, Fouirer Optics, Roberts and Company Publishers, 2005.

[37] D. J. Schroeder, Astronomical Optics, Academic Press, 1999.

[38] James E. Harvey, Christ Ftaclas, "Diffraction effects of telescope secondary mirror spiders on various image-quality crietri," *Applied Optics,* vol. 34, no. 28, pp. 6337-6349, 1995.

[39] Ken-ichiro Murata, Hajime Tanaka, "Surface-wetting effects on the liquid-liquid transition of a single-component molecular liquid," *Nature Communications,* vol. 1, no. 16, pp. 1-9, 2010.

[40] H.-J. Kunze, Introduction to Plasma Spectroscopy, Springer, 2009.

[41] J.-B. Sirve, B. Bousquet, L. Canioni, L. Sarger, "Time-resolved and time-integrated single-shot laser-induced plasma experiments using nanosecond and femtosecond laser pulses," *Spectrochimica Acta Part B,* vol. 59, no. 7, pp. 1033-1039, 2004.

[42] Thomas Justel, Jean-claude Krupa, Detlef U. Wiechert, "VUV spetroscopy of luminescent materials for plasma display panels and Xe discharge lamps," *Journal of Luminescence,* vol. 93, pp. 179-189, 2001.

[43] Hakaru Mizoguchi, Hiroaki Nakarai, Tamotsu Abe, Takeshi Ohta, Krzysztof M Nowak, Yasufumi Kawasuji, Hiroshi Tanaka, Yukio Watanabe, Tsukasa Hori, Takeshi Kodama, Yutaka Shiraishi,Tatsuya Yanagida, Tsuyoshi Yamada, Taku Yamazaki,Shinji Okazaki, Takash Sait, "LPP-EUV Light Source Development for High Volume Manufacturing Lithography," in *SPIE*, 2013.

[44] C. W. Gwyn, R. Stulen, D. Sweeney, D. Attwood, "Extreme ultraviolet lithography," *Journal of Vacuum Science & Technology B,* vol. 16, no. 6, pp. 3142-3149, 1998.

[45] Patrick Cogez, Mart Graef, Bert Huizing, Reinhard Mahnkopf, Hidemi Ishiuchi, Junji Shindo, Siyoung Choi, Jae Hoon Choi, Carlos H. Diaz, Yee Chaung See, Bob Doering, Paolo Gargini, Taffy Kingscott, Ian Steff, "International Technology Roadmap for Semiconductors," in *ITRS*, 2012.

[46] Hideaki Hashimoto, Nobutaka Kikuiri, Eiji Matsumoto, Hideo Tsuchiya, Riki Ogawa, Ikunao Isomura, Manabu Isobe, Kenichi Takahara, "Improvement of a DUV mask inspection tool to hand over the baton for next-generation tool smoothly," in *SPIE*, 2013.

[47] P. J. Silverman, "Extreme ultraviolet lithography: owverview and development status," *Journal of Micro/Nanolithography, MEMS, andn MOEMS,* vol. 4, no. 1, p. 011006, 2005.

[48] B. Vivek, EUV sources for lithography, SPIE Press, 2006.

[49] Junichi Fujimoto, Tamotsu Abe, Satoshi Tanaka, Takeshi Ohta, Tsukasa Hori, Tatsuya Yanagida, Hiroaki Nakarai, Hakaru Mizoguchi, "Laser-produced plasma-based extreme-ultraviolet light source technology for high-volume manufacturing extreme-ultraviolet

lithography," *Journal of Micro/Nanolithography, MEMS, and MOEMS,* vol. 11, no. 2, p. 021111, 2012.

[50] S.-G. Crystals, "BaF2 Barium Fluoride Scintillation Material".

[51] Arisato Ejiri, Sinzouo Kubota, Akira Hatano, Kazuhisa Yahagi, "Vacuum UV Photoelectric Yield Spectra of BaF2 and SrF2 Crystals," *Journal of the Physical Society of Japan,* vol. 64, no. 5, pp. 1484-1488, 1995.

[52] Ted Liang, Edita Tejnil, Alan Stivers, "Pattern Inspection of EUV Masks Using DUV Light," in *SPIE*, 2002.

[53] I. Mochi, K. A. Goldberg, B. La Fontanie, A. Tchikoulaeva, C. Holfeld, "Actinic imaging of native and programmed defects on a full-field mask," in *SPIE*, 2010.

[54] Moza Al-Rabban, Martin Richardson, Howard Scott, Franck Gilleron,Michel Poirier, Thomas Blenski, "Modeling LPP Sources," in *EUV sources for lithography*, SPIE Press Monograph, 2006, p. Chapter 10 .

[55] M. Richardson, C.-S. Koay, K. Takenoshita, C. Keyser, S. George,M. Al-Rabban, and V. Bakshi, "Laser Plasma EUV Sources Based on Droplet Target Technology," in *EUV sources for lithography*, SPIE Press Monograph, 2006, p. Chapter 26.

[56] F. Jin, M. Richardson, "New laser plasma source for extreme-ultraviolet lithography," *Applied Optics,* vol. 34, no. 25, pp. 5750-5760, 1995.

[57] M. C. R. Glenn D. Kublak, "Cluster beam targets for laser plasma extreme ultraviolet and soft X-ray sources". United States of America Patent US5577092 A, 19 November 1996.

[58] David Torres, Feng Jin, Martin C. Richardson, Chris DePriest, "Characterization of mass-limited ice droplet laser plasmas," *Trends in Optics and Photonics Extreme Ultraviolet Lithography,* vol. 4, pp. 75-79, 1996.

[59] Feng Jin, Martin C. Richardson, Gregory Shimkaveg, David Torres, "An advanced EUV source from water droplet laser plasma," *Trends in Optics and Photonics Extreme Ultraviolet Lithography,* vol. 4, pp. 89-91, 1996.

[60] David Torres, Chris DePriest, Martin C. Richardson, "A debris-less laser plasma source for EUV and XUV generation," *Topographical Meeting on High Field & Short Wavelength Sources,* vol. 7, pp. 175-177, 1997.

[61] Martin C. Richardson, David Torres, Chris DePriest, Feng Jin, Gregory Shimkaveg, "A Debris-Free Laser-Plasma EUV Source Using Ice Droplets," in *SPIE*, 1997.

[62] Richardson, M.; Torres, D.; DePriest, C.; Jin, F.; Shimkaveg, G., "Mass-limited, debris-free laser-plasma EUV source," *Optics Communications,* vol. 145, no. 1-6, pp. 109-112, 1998.

[63] Guido Schriever, Martin C. Richardson, I.C.E. Turcu, "The droplet laser plasma source for EUV lithography," in *CLEO*, 2000.

[64] Guido Schriever, Christian Keyser, Martin C. Richardson, "Debris-free, droplet loser plasma sources in the EUV and soft X-ray ranges," in *I.C.E. Turcu, International Quantum Electronics Conference*, 2000.

[65] Martin C. Richardson, Christian Keyser, Moza Mohammad Al-Rabban, Robert Bernath, "Dynamics of mass-limited laser plasma targets as sources for EUVL," in *International Microprocesses and Nanotechnology Conference*, 2001.

[66] Christian Keyser, Chiew-Seng Koay, Robert Bernath, Martin C. Richardson, I.C.E. Turcu, Harry Rieger, Mike F. Powers, "Liquid Droplet-Target Laser Plasma Sources for EUV Lithography," in *CLEO*, 2002.

[67] Chiew-Seng Koay, Christian Keyser, Martin C. Richardson, "Developments in point sources for EUV lithography," in *International Quantum Electronics Conference*, 2002.

[68] Kazutoshi Takenoshita, Chiew-Seng Koay, Martin C. Richardson, I.C.E. Turcu, "The repeller field debris mitigation approach for EUV sources," *Emerging Lithographic Technologies VII, SPIE,* vol. 5037, pp. 792-800, 2003.

[69] Keyser, C.; Schriever, G.; Richardson, M.; Turcu, E., "Studies of high-repetition-rate laser plasma EUV sources from droplet targets," *Applied Physics a-Materials Science & Processing,* vol. 77, no. 2, pp. 217-221, 2003.

[70] Chiew-Seng Koay, Christian Keyser, Kazutoshi Takenoshita, Moza Mohammad Al-Rabban, Martin C. Richardson, I.C.E. Turcu, Harry Rieger, A. Stone, J. H. Morris, "High conversion efficiency tin material laser plasma source for EUVL," *Emerging Lithographic Technologies VII, SPIE,* vol. 5037, pp. 801-806, 2003.

[71] Christian Keyser, Chiew-Seng Koay, Kazutoshi Takenoshita, Martin C. Richardson, I.C.E. Turcu, "High conversion efficiency mass-limited laser plasma source for EUV lithography," in *CLEO*, 2003.

[72] Christian Keyser, Robert Bernath, Moza Al-Rabban, Martin Richardson, "Dynamics of Mass-limited, Laser Plasma Targets as Sources for EUV Lithography," *Japanese Journal of Applied Physics,* vol. 41, 2003.

[73] Chiew-Seng Koay, Kazutoshi Takenoshita, Etsuo Fujiwara, Moza Mohammad Al-Rabban, Martin C. Richardson, "Spectroscopic studies of the Sn-based droplet laser plasma EUV source," *Proceedings of SPIE, Emerging Lithographic Technologies VIII,* vol. 5374, pp. 964-970, 2004.

[74] Martin C. Richardson, Chiew-Seng Koay, Kazutoshi Takenoshita, Christian Keyser, Simi A. George, Somsak (Tony) Teerawattanasook, Moza Mohammad Al-Rabban, H. Scott,

"Laser plasma EUVL sources – progress and challenges," *roceedings of SPIE, Emerging Lithographic Technologies VIII,* vol. 5374, pp. 447-453, 2004.

[75] Hideaki Hashimoto, Nobutaka Kikuiri, Eiji Matsumoto, Hideo Tsuchiya, Riki Ogawa, Ikunao , "Improvement of a DUV mask inspection tool to hand over the baton for next-generation tool smoothly," in *SPIE*, 2013.

[76] G. K. B. W. Anatoly Romanovsky, "Extending the lifetime of a deep UV laser in a wafer inspection tool". United States of America Patent US8432944 B2, 30 April 2013.